

1 **The response of the Subtropical Front to changes in the Southern Hemisphere Westerly Winds –**
2 **Evidence from models and observations.**

3 Erik Behrens¹, Helen Bostock²

4 ¹ National Institute of Water and Atmospheric Research, Wellington, New Zealand

5 ² The University of Queensland, Brisbane, Australia

6

7 Corresponding author: Erik Behrens, erik.behrens@niwa.co.nz

8

9 Key points:

- 10 • Stronger (Weaker) westerly winds shift the location of the Subtropical Front northward
11 (southward), except in regions of strong currents.
- 12 • The observed shift of the Subtropical Front (2004-2019) is smaller than the shift in the westerly
13 winds, due to increased Ekman transport.
- 14 • Satellites show that southward shifts of the STF trigger a positive (negative) chlorophyll-a
15 response south (north) of the front.

16 **Abstract:**

17 The location of the Subtropical Front (STF), the boundary between Subtropical and Subantarctic Water
18 in the Southern Ocean is proposed to be controlled by the strength and location of the Southern
19 Hemisphere westerly winds. We use a hydrodynamic hindcast model and recent observations to test
20 if changes in the westerly winds can cause meridional shifts in the STF over interannual to decadal
21 time scales by modulating local Ekman transport. We find that increased, or northward, shifted
22 westerly winds lead to an enhanced northward Ekman transport over large parts of the Southern
23 Ocean, resulting in a northward shift in the STF. Conversely for weaker or southward shifted westerly
24 winds. Regions with strong eddy variability, such as western boundary current systems of the Agulhas
25 and East Australian Current behave differently, as the Sverdrup balance causes an opposite shift. In
26 these regions an increase in westerly winds lead to a southward shift in the STF. A southward shift of
27 STF has been observed between 2004-2019. However, the shift is smaller than the latitudinal shifts in
28 the location of the zero wind stress curl and maximum westerly winds (-0.4° latitude/decade). This
29 discrepancy is due to positive Ekman trends resulting from the intensification of the westerly winds,
30 which oppose the southward migration. Changes in the Ekman transport and the overall southward
31 shift of the STF have also resulted in an observed positive trend in chlorophyll-a concentrations south
32 of the STF, which could have ramifications for the biological pump and carbon uptake in the Southern
33 Ocean.

34

35 **Plain English Abstract:**

36 The Subtropical Front (STF) is an important water mass barrier, between warm, salty and nutrient-
37 depleted Subtropical Waters of the subtropical gyre to its north, and cold, fresh, but nutrient-rich
38 Subantarctic Waters of the Southern Ocean to its south. The position of the STF is thought to be
39 controlled by the westerly winds. In this study we investigate if the STF shifts with changes in these
40 westerly winds. Our model experiments show that over large parts of the Southern Ocean, the

41 changes in the location of the STF follow changes in the westerly winds, except in regions of strong
42 oceanic currents. The observations show that between 2004-2019 a small southward trend of the STF
43 has been detected over most parts of the Southern Ocean as a consequence of southward shift of the
44 westerly winds due to positive Southern Annular Mode (SAM). However, the shift in the STF has not
45 been as large as the shift in the winds, as it has been opposed by the strengthening of the westerly
46 winds. The recent southward shift in the STF has led to an increase in plankton growth south of the
47 STF due to increased mixing of the Subtropical and Subantarctic Waters.

48 **1. Introduction**

49 The Subtropical Front (STF) marks the water mass boundary between warm, salty but nutrient-
50 depleted Subtropical Water in the subtropical gyre to its north, and cold, fresh, and nutrient-rich
51 Subantarctic Waters in the Southern Ocean to its south (Belkin 2021; Belkin and Gordon 1996;
52 Chapman et al. 2020; Deacon 1982; Orsi et al. 1995; Sokolov and Rintoul 2009). As such the STF is
53 often used as the northern boundary of the Southern Ocean. Due the mixing of these two water
54 masses the STF is a hotspot for primary production seen by elevated levels of chlorophyll-a (Chiswell
55 et al. 2013; Pinkerton et al. 2005; Sullivan et al. 1993; Weeks and Shillington 1994), and therefore also
56 important for carbon sequestration and fisheries.

57 The location of the STF is proposed to be controlled by the strength and location of the Southern
58 Hemisphere westerly winds. However, the exact position of the STF is still not fully understood, since
59 its location does not align with the theory that it should co-locate with the line of zero wind stress curl
60 (De Boer et al. 2013; Tilburg et al. 2002). This knowledge gap has motivated a range of research and
61 has led to an alternative definition of the Subtropical Front, the so called Dynamical Subtropical front,
62 which links the STF to ocean dynamics rather than water mass properties (De Boer et al. 2013; Graham
63 et al. 2012). Furthermore, recent research suggests that the STF will show a poleward shift as a
64 consequence of expanding subtropical gyres due to positive Southern Annual Mode (SAM) trends
65 shifting the southern hemisphere westerly winds south over multi-decadal timescales (Yang et al.
66 2020). However, equatorward shifts of the STF have also been reported, challenging the potential
67 drivers of shorter, sub-decadal shifts (Yang et al. 2020).

68 In this paper we investigate the drivers of STF variability on interannual to decadal timescales using a
69 combination of Argo, satellite, and hindcast datasets. Here we define the STF by the 11°-isotherm at
70 100m depth following Orsi et al. (1995). In particular we test if changes in STF location can be
71 attributed to local changes in the Ekman transport, as a consequence of changes in the westerly winds
72 (meridional shift, or changes in the strength of the winds, Figure 1).

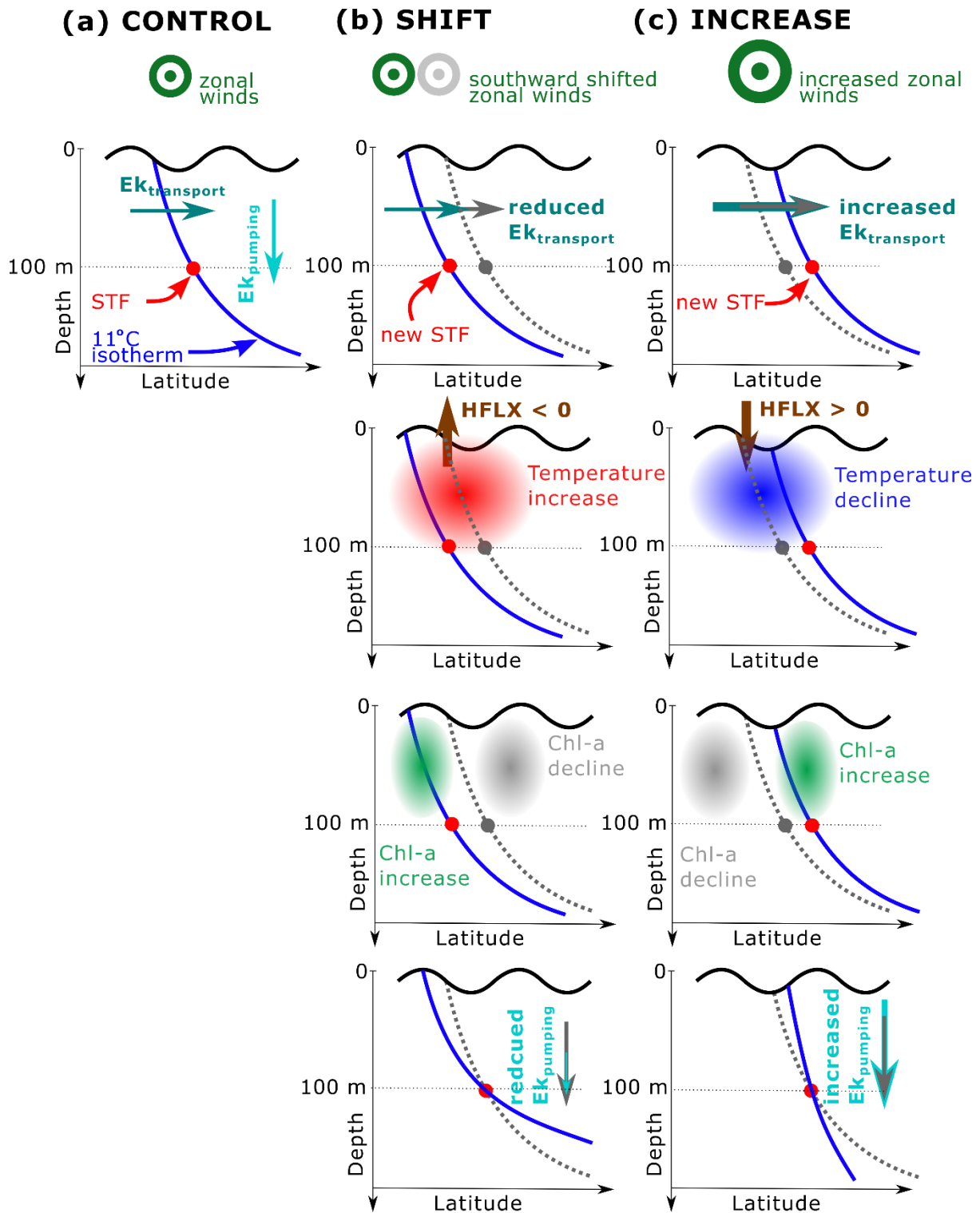
73 In theory an increase in surface (zonal) winds would result in a stronger local Ekman transport (Figure
74 1b), which carries more cold Subantarctic Waters northward and would trigger a northward shift of
75 the STF. The negative sea surface temperature (SST) anomalies would cause a positive heat flux
76 anomaly (into the ocean) trying to compensate for the advection of cold water northward. Associated
77 changes in the wind stress curl increase the Ekman pumping north of the STF and results in steeper
78 isotherms, but may not necessarily generate a shift in the STF at 100m depth. Furthermore, these
79 negative SST anomalies would lead to negative chlorophyll-a (Chl-a) anomalies in Subantarctic Waters
80 (temperature response) and an increase in Subtropical Waters (nutrient response), relative to the
81 mean location of the STF. This concept follows previous work in the Southern Ocean (Lovenduski
82 2005), but has been applied to the STF in this paper.

83 In the case of southward shifting winds (Figure 1c) local Ekman transport declines, which initiates a
84 southward shift of the STF. Consequently, that leads to negative heat flux anomalies (out of the ocean)

85 and an increase in Chl-a concentration to the south of the STF and a decline to its north. However, a
86 reduction in Ekman pumping north of the STF shoals the isotherms, however, again it may not impact
87 the location of the STF at 100m water depth.

88 In this paper we use hydrodynamic hindcast and idealized simulations with individual changes to the
89 wind forcing using the NZ20 model (Behrens et al., 2021) in combination with in-situ and remote
90 sensing observation data from 2004-2019 to test these conceptual models (Figure 1).

91 The paper is organised as follows: Section 2 introduces the data sources and methods. Section 3.1
92 summaries the results from sensitivity simulations where surface winds have been deliberately
93 altered. Section 3.2 highlights where Ekman transports can be used to explain interannual variability
94 of the STF in the Southern Ocean between 2004-2019 and section 3.3 provide insights into long-term
95 trends. Section 4 provides a conclusion.



96

97 Figure 1: This Schematic shows how changes in surface winds would alter the location of the STF. (a)
 98 for the CONTROL, (b) for a southward shift of the westerly winds and (c) for an increase in westerly
 99 winds in relation to CONTROL. The blue lines mark the 11°-isotherm and the red dots showing the
 100 location of the STF at 100 m depth (as defined by Orsi et al. (1995)). In b) and c) the grey dotted lines,
 101 grey dots, and grey circles are the 11° C isotherm, STF location and winds from the CONTROL case. In
 102 (b) a southward shift of the winds leads to negative Ekman transport anomalies, and a southward shift
 103 of the STF accompanied by positive temperature anomalies. These temperature anomalies trigger
 104 positive heat flux anomalies (HFLX, from the ocean to the atmosphere) and cause a decline of Chl-a

105 north of the STF_{CONTROL} and an increase to its south. However, reduced Ekman pumping shoals the
106 isotherms, but may not impact the location of the STF. (c) An increase in the strength of the westerly
107 winds leads to positive Ekman transport anomalies, and a southward shift of the STF accompanied by
108 negative temperature anomalies and negative heat flux anomalies (from the atmosphere into the
109 ocean). The negative SST anomalies results in negative Chl-a anomalies south of the STF_{CONTROL} and
110 positive anomalies to the north. An increase in Ekman pumping results in a steepening of the
111 isotherms, but may not shift the STF.

112 **2. Methods**

113 **2.1 Model simulation**

114 This study uses data from a high-resolution (1/20°) nested ocean - sea-ice hindcast (Behrens et al.
115 2021). Ocean physics are simulated by NEMO 3.6 (Madec et al. 2017), while CICE version 5.2.1 (Hunke
116 and Lipscomb 2010) has been used for sea-ice. The base for the nested model is a global eddy
117 permitting configuration, with a nominal resolution of ¼° degree, which is known as GO6, and details
118 of this configuration for this global setup can be found in Storkey et al. (2018). The nested region spans
119 the ocean around New Zealand from 142.8°E to 152°W and 59°S to 22°S with a grid spacing of about
120 4km to fully resolve mesoscale processes (and to partially resolve sub-mesoscale dynamics). This
121 nested model setup has been used in a related study to investigate, past variability of the STF around
122 New Zealand (Behrens et al. 2021) and demonstrated a better performance than the global
123 configuration without a nested region. The nesting has been facilitated by a two-way nesting scheme
124 based on AGRIF (Debreu et al. 2008). The vertical dimension is discretized by 75-vertical z-levels, with
125 a 1 m thick surface layer which increases to about 200 m in the deep ocean. The model uses a non-
126 linear free surface and a partial cell approach to improve bottom flows (Barnier et al. 2006). This model
127 simulates boundary current transports (supplementary material, Table 1) and the STF (Belkin 2021) in
128 good agreement to observations.

129 In this nested setup a 62-year long model hindcast, from 1958 to 2019 has been conducted, using
130 JRA55-DO v1.5 (Tsuji et al. 2018) atmospheric boundary conditions, hereafter CONTROL. The
131 simulation has been started from rest with temperature and salinity fields based on the EN4
132 climatology (Good et al. 2013). A coastal runoff climatology has been applied, and sea surface salinity
133 has been restored to the EN4 climatology with time scales of 30 days for the 1 m thick surface layer.
134 In addition to the CONTROL, two sensitivity simulations have been conducted where changes to the
135 surface winds, between 70°S to 25°S, have been applied. These simulations cover the period from
136 2000-2019 to test how changes in the surface winds impact the location of the STF. It is assumed that
137 a period of 20 years is sufficient to detect a robust response in these sensitivity simulations in
138 comparison to CONTROL.

139 In the first simulation the winds (zonal and meridional) are shifted south by 1-degree latitude per
140 decade, hereafter SHIFT. Applying the anomalies to zonal and meridional winds, reduces the distortion
141 of storms, which can otherwise result in artificial wind-stress curl anomalies (Frankcombe et al. 2013).
142 In the second simulation an increase in zonal and meridional winds, hereafter INCREASE, of 1% per
143 year has been applied, which reflects an increase of wind speeds by 20% at the end of 2019. Applying
144 trends instead of step changes to winds, as done in previous studies (Frankcombe et al. 2013; Spence
145 et al. 2010; Spence et al. 2014), was motivated to avoid initial shocks and to reduce the likelihood of
146 spurious deep convection in the Southern Ocean (Behrens et al. 2016), which could also influence the
147 STF response to these wind perturbations. The JRA55-DO v1.5 winds show over the period 2000-2019
148 in CONTROL an increasing trend in zonal winds between 0 to 0.6% per year, which varies by latitude
149 (supplementary material, Figure S1). Over this period the location of the maximum of the zonal winds

150 also shows a southward trend of 0.4 degrees latitude per decade. These JRA55-DO values are in-line
151 with previous estimates (see Swart and Fyfe 2012). The imposed trends in the experiments SHIFT and
152 INCREASE are larger than the observed trends between 2000 and 2019 and intended to simulate the
153 general response to shifted or increased winds. However, there are some possible issues with forced
154 models as the unavoidable thermal restoring (due to unchanged air temperatures) might limit the STF
155 response to artificial wind changes.

156 **2.2 Additional data sources and metrics**

157 The Roemmich-Gilson Argo climatology (Roemmich and Gilson 2009), hereafter referred to as Argo,
158 has been used for the comparison to model temperatures and model STF location. Furthermore, Chl-
159 a from MODIS satellite (Sathyendranath et al. 2019) mission has been used to link Chl-a anomalies to
160 meridional shifts in the location of the STF. The monthly mean MODIS satellite data was linearly
161 interpolated onto a regular $1^\circ \times 1^\circ$ grid to allow for a direct comparison to the Argo results, which are
162 also provided on a regular $1^\circ \times 1^\circ$ grid.

163 We apply the Orsi et al. (1995) definition to locate the STF, which uses the 11°C isotherm at 100m
164 depth. By using temperatures at 100m depth to define the STF instead of using SSTs the seasonal
165 variability is reduced (Orsi et al. 1995). Furthermore, temperature anomalies over the top 100m have
166 been calculated to link them to Ekman transports and to meridional shifts of the STF. Using the top
167 100m averaged temperature was motivated by Ekman depths of about 75m - 100m at this latitude
168 (Lenn and Chereskin 2009; Wang and Huang 2004), and the STF defined as the 11°C isotherm at 100m.
169 This choice also reduces the impact of the SST ‘restoring’ of ocean-only models. All data sources
170 (model and observational data) are available as monthly means, but were annually averaged to
171 investigate interannual variability between years.

172 For the two wind perturbation sensitivity simulations, we have evaluated meridional shifts of the STF,
173 Ekman transports, surface heat fluxes and Ekman pumping over the entire Southern Ocean. We focus
174 on the data over the last 5 years of the simulation (2015-2019) relative to the CONTROL simulation to
175 detect forcing related changes over intrinsic variability.

176 To test the STF response, following Figure 1, anomalies for the top 100m temperatures, surface heat
177 fluxes, Ekman transports, Ekman pumping, mixed layer depths (MLD), potential vorticity and
178 meridional 100m temperature gradient have been computed over a latitudinal range of $\pm 2.5^\circ$ latitude
179 over the mean STF location (2004-2019, hereafter $\text{STF}_{\text{CONTROL}}$). MLDs have been identified as depths
180 where the potential density difference exceeds 0.01 kg/m^3 compared to the surface layer. Potential
181 vorticity has been calculated using the local Coriolis parameter divided by the local water depth. Chl-
182 a anomalies have been computed for a 5° latitude band south of the mean STF location. In addition,
183 we have zonally averaged all data sources in 5° longitude bands.

184 **3. Results and discussion**

185 **3.1. Wind sensitivity simulations**

186 Both SHIFT and INCREASE simulations show changes in the location of the STF of $\pm 2^\circ$ in latitude over
187 the last 5 years (2015-2019) in comparison to CONTROL (Figure 2a-b). In INCREASE (blue lines) the
188 displacement of the STF is predominantly northward, in agreement with Figure 1. In SHIFT, the STF
189 migrates predominantly southward, but considerably less than expected compared to the applied 2°
190 degree shifted winds by the end of 2019. In both sensitivity simulations the STF response is not-
191 uniform with longitude (Figure 2b). Furthermore, the magnitude of meridional displacement in either
192 INCREASE or SHIFT simulations is not linked to changes in ocean bathymetry (black line here

193 represented by potential vorticity). This differentiates the surface intensified STF from other fronts in
194 the Southern Ocean, which are directly influenced by bottom topography due to their barotropic
195 nature (Thompson and Sallée 2012). The regions where the sign of the STF anomaly aligns with the
196 sign of the Ekman anomaly (Figure 1) are represented by the horizontal bars at the top of Figure 2b.
197 In SHIFT the STF response follows the proposed Ekman transport (red horizontal bar in Figure 2b) over
198 parts of the Agulhas region, the central Indian Ocean, south of Australia to 160°E, over small parts of
199 the central Pacific Ocean (~130°W), the eastern Pacific Ocean and east of the Malvinas Current. In
200 INCREASE, similar regions to SHIFT show an agreement between the STF response and the Ekman
201 transport (blue horizontal bar), but not for the western boundary currents. The different behavior for
202 the boundary currents can be explained by the Sverdrup balance, with an increase in basin-wide wind
203 stress curl in INCREASE (Figure S4c). That leads to an increase in the strength of the western boundary
204 currents, which shifts the STF southward in these regions, against the local enhanced northward
205 Ekman forcing (Figure S2c). In SHIFT the impact on western boundary currents and open ocean is the
206 same and both tend to shift south.

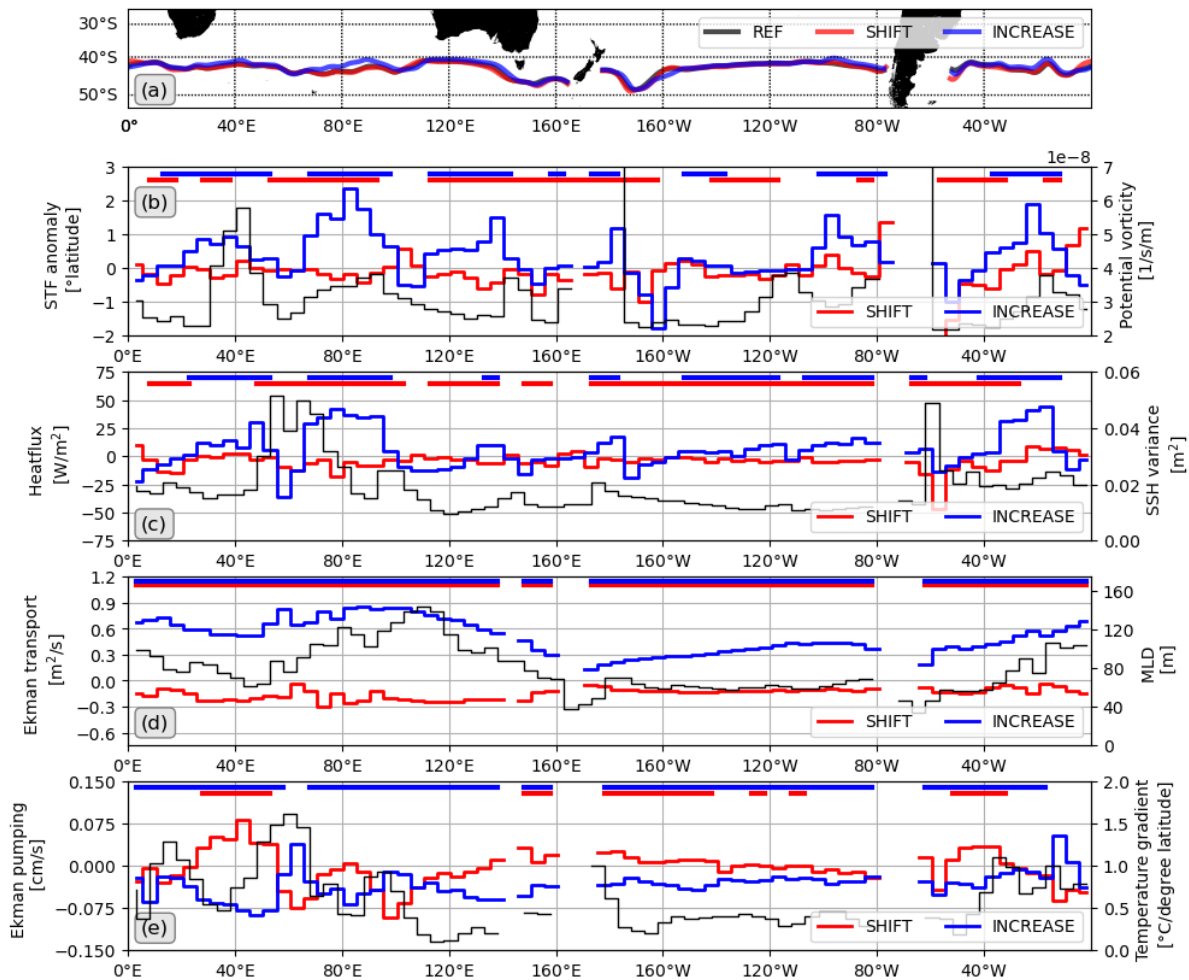
207 The surface heat flux anomalies (Figure 2c) over the STF_{CONTROL} co-vary in most regions with the sign
208 and magnitude of the STF displacement from Figure 2b in SHIFT (red horizontal bar). In INCREASE,
209 exceptions occur in regions of high mesoscale activity, illustrated by sea surface height variance (black
210 line in Figure 2c). Regions of high mesoscale activity are between 60°-70°E, part of the Agulhas Return
211 Current, around 100°E where a branch of the Super Gyre crosses the STF, around 150°E where the
212 East Australian Current Extension overshoots, around 180° where the STF detaches from the Chatham
213 Rise, around 110°W in middle of the Pacific Ocean and at 30°W within the Malvinas Current. These
214 regions of alignment with Figure 1 overlap with regions identified in Figure 2b.

215 The sign of the induced Ekman transport anomalies aligns with Figure 1 (horizontal bars in Figure 2d
216 and see Figure S2), while the magnitude varies zonally due to the actual strength of the zonal winds
217 and the pathway of the STF. The magnitude of the Ekman transport anomalies does not correlate with
218 the magnitude of meridional STF shift, locally. Nevertheless, the overall Ekman transport anomaly in
219 INCREASE is larger in comparison to SHIFT and consequently a larger STF displacement is seen in
220 INCREASE compared to SHIFT. Furthermore, the largest Ekman transport anomalies are located over
221 the Indian Ocean in INCREASE and SHIFT, which is also the ocean basin showing the largest meridional
222 STF shift. In addition, this is also the region with the deepest MLDs for the STF of about 130m (black
223 curve). MLDs of about 100m or deeper would allow that surface heat flux anomalies and heat
224 advection to directly influence the location of the STF, while shallower MLDs would prevent this direct
225 impact. MLDs over the central Pacific and eastern Pacific Ocean are only 60m deep, which may explain
226 the smaller STF changes in the Pacific Ocean. This would suggest that surface heat fluxes and heat
227 advection alone cannot penetrate deep enough to impact the STF directly, and potentially limit the
228 STF response in these regions.

229 The Ekman pumping response aligns with Figure 1 for INCREASE for most longitudes, but less so for
230 SHIFT (Figure 2e, see also Figures S4-S5). Reasons for the discrepancy in SHIFT might be due to an
231 overall smaller applied perturbation in SHIFT, compared to INCREASE, which might not be large
232 enough to overcome the intrinsic variability. The meridional temperature gradient (black line) is
233 elevated in regions with higher mesoscale variability and restricts the meridional shift of the STF. A
234 smaller meridional temperature gradient would allow for a larger meridional displacement of the STF
235 with the same perturbation.

236 Overall, these sensitivity tests suggest a link between STF displacement and local Ekman transport in
237 regions away from energetic western boundary currents. While the direction of displacement follows
238 the sign of the Ekman transport anomalies, the local magnitude of STF displacement cannot be directly

239 attributed to the magnitude of Ekman transport anomaly. Here, the local oceanographic conditions,
 240 such as horizontal temperature gradient and presence of oceanic currents also impact the magnitude
 241 of the displacement. The applied wind anomalies are stronger than the observed natural trends and
 242 therefore the initiated response might be stronger than in the real world. Nevertheless, the actual
 243 modelled STF response to these wind anomalies was weaker than expected due to the dampening
 244 effect of the thermal restoring, by prescribing the same SSTs across all simulations. We have defined
 245 the STF by the 11°C isotherm at 100m depths (Orsi et al., 1995), which reduces the impact of the
 246 thermal restoring. However future studies could use fully coupled models to evaluate the STF
 247 response to these wind changes to eliminate this shortcoming.



248

249 Figure 2: 2015-2019 anomalies for INCREASE and SHIFT relative to CONTROL: (a) STF location, (b) STF
 250 location anomaly and potential vorticity (f/h) from CONTROL, (c) surface heat flux anomaly and mean
 251 sea surface height (SSH) variance from CONTROL, (d) Ekman transport anomaly and mean mixed layer
 252 depth (MLD) from CONTROL, (e) Ekman pumping anomaly and meridional 100m temperature gradient
 253 from CONTROL. The anomalies are computed over the mean path ($\pm 2.5^\circ$ latitude) of the STF_{CONTROL}.
 254 The straight coloured bars at the top indicate where the sign of anomalies align with the Figure 1
 255 schematic. Results in (b)-(e) have been binned to 5° longitude bins.

256 3.2. Drivers of interannual observed variability of the STF

257 In this section we test if and where this above-described physical conceptual model can be applied to
 258 understand the observed interannual variability of the STF between 2004-2019 using temperature
 259 from Argo floats (Argo data only available from 2004 onwards), and the biological response through

260 satellite observed Chl-a anomalies. In doing so we aim to identify regions where Ekman transport can
261 explain past STF variability, and regions where other drivers are at play.

262 The observed top 100m temperature anomalies from Argo show interannual variations in the order
263 of $\pm 0.8^{\circ}\text{C}$ and an overall positive trend over the period 2004 to 2019 (Figure 2a and see section 3.3).
264 The modelled top 100m temperature anomalies align with the observed anomalies (Figure 2b) in time,
265 space and magnitude for most regions. This good match suggests a good performance of NZ20 to
266 simulate past STF variability. The exception is large fluctuations on spatial and interannual scales
267 between 0 and 60°E , which is the region impacted by the Agulhas Retroflexion and Return Current.

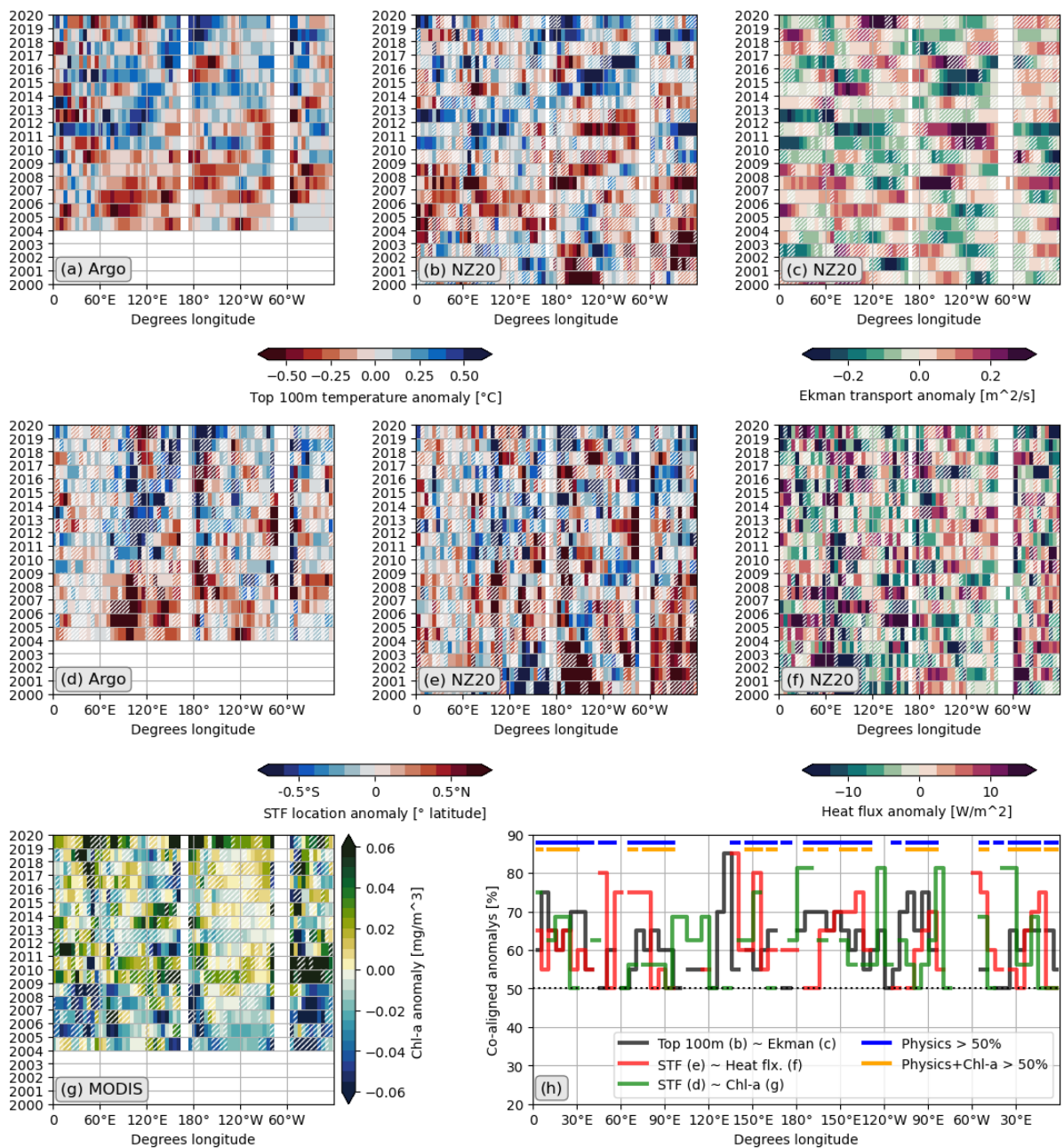
268 In particular, the larger modelled temperature anomalies ($<-0.5^{\circ}\text{C}$, $>0.5^{\circ}\text{C}$) co-align with the sign of
269 the model Ekman transport anomalies (non-hatched anomalies in Figure 2b and 2c) as expected from
270 Figure 1. In addition, the magnitude of the Ekman transport anomalies appears to be reflected in the
271 magnitude of the temperature anomalies. The top 100m temperature anomalies consequently
272 generate a very similar pattern in the meridional displacement of the STF (Figure 2d-e) in Argo and in
273 the model. The modelled surface heat fluxes over the STF (Figure 3f) exhibit more variability in space
274 and time than the Ekman transports (Figure 3c). This suggests that the observed heat fluxes are not
275 entirely driven by Ekman transports alone as they are in both sensitivity simulations SHIFT and
276 INCREASE. In the real-world wind changes also influence surface air temperature anomalies via
277 advection and impact heat flux anomalies. Despite the larger variability, the sign of surface heat flux
278 anomalies and modelled STF displacement aligns with what is expected in Figure 1 in many regions,
279 as shown in Figure 3e,f by the non-hatched anomalies.

280 Now we assess the biological response in relation to shifts of the STF, by analyzing Chl-a anomalies up
281 to 5° south of the mean location of the STF (Figure 2g). For most longitudes there is a positive Chl-a
282 trend, which corresponds to the positive temperature trend (Figure 2a and section 3.3) and an overall
283 southward shift of the STF (Figure 2d) between 2004-2019. The sign of Chl-a and STF anomalies on
284 shorter, interannual timescales aligns in many cases with the concept in Figure 1 (non-hatched
285 anomalies in Figure 2d,g). This is particularly true for strong (<-0.5 or $>0.5 \text{ mg/m}^3$) Chl-a anomalies.

286 To assess the overall robustness of the concept in Figure 1 a simple counting of anomalies which follow
287 the concepts in Figure 1 has been performed over the Southern Ocean for the observed and modelled
288 data between 2004 and 2019 (Figure 2g). The small sample size (16 annual values from 2004 to 2019)
289 restricted more sophisticated methods to be deployed to measure its robustness. Neither, a Pearson
290 nor a Spearman correlation produced significant ($>95\%$ significant level) relationships for any of the
291 parameters. Nevertheless, the counting suggest that the concepts of Figure 1 apply between 60-80%
292 of the time over large parts of the Southern Ocean. Regions where the physical concept follows the
293 concept in Figure 1 (likelihood $\geq 50\%$ for both physical criteria) are shown by the blue horizontal bar
294 and account for about 75% of the ocean. Regions where the physical concept fails align with regions
295 identified in Figure 2c (black line), where mesoscale eddy variability is elevated, for example at around
296 60°E and 120°E where the STF interacts with the Agulhas Return Current and the southern boundary
297 of the Super Gyre, respectively. The Syper Gyre is the combination of the three subtropical gyres in
298 the Southern Hemisphere, diagnosed by the zero line of the barotropic streamfunction, which
299 spearates the subtropics from the Antarctic Circumpolar Current.

300 If we include Chl-a in the assessment criteria with the physical criteria (orange bars, likelihood $\geq 50\%$
301 for all three criteria), the concept still applies to about 50% of the ocean. We acknowledge that the
302 50% cut-off threshold is an arbitrary choice to prove that the concept applies since an independent
303 normal distributed process should center around 50%. Nevertheless, since these processes are
304 biophysically linked, the probability that they randomly co-occur are unlikely. The geographical

305 coherence of this agreement and disagreement provides further evidence that the concept applies in
 306 many regions. This concept fails in regions where the STF interacts with strong western boundary
 307 currents and subsequent elevated eddy activity.



308

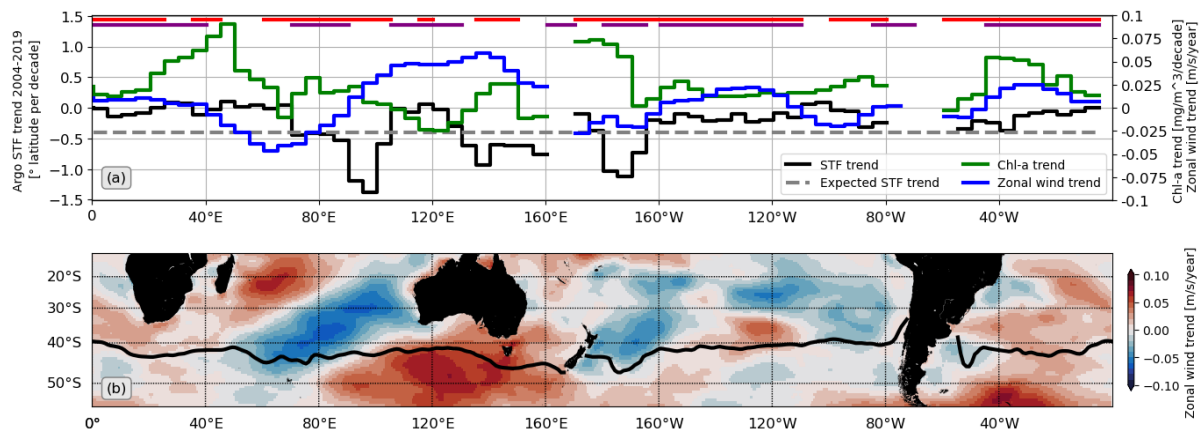
309 Figure 3. (a) Top 100m Argo temperature anomaly relative to the period 2004-2019 (b) Same as (a)
 310 but for NZ20. (c) NZ20 Ekman transport anomaly. Hatching in (b) and (c) indicates where the sign of
 311 top 100m temperature and Ekman transport anomalies does not align with the concept in Figure 1.
 312 (d) Argo meridional STF location anomaly in ° latitude. (e) same as (d) but for NZ20. (f) surface heat
 313 flux anomalies from NZ20 where positive anomalies indicate a heat flux into the ocean. Hatching in
 314 (e) and (f) indicates where the sign of STF location and surface heat fluxes anomalies does not align
 315 with the concept in Figure 1. (g) MODIS chlorophyll-a anomaly. Hatching in (d) and (g) indicates where
 316 the sign of chlorophyll-a and Argo STF anomalies does not align with the concept in Figure 1. (h) How
 317 often anomalies align between Ekman transport versus top 100m temperature in NZ20 (black), heat
 318 flux anomalies versus STF anomalies from NZ20 (red) and Argo STF anomalies and Chl-a anomalies

319 (green) with the concept from Figure 1. Blue (orange) bar indicates where the black and red (and
 320 green) line shows at least an agreement of $\geq 50\%$ over time. All anomalies (a) - (f) are extracted over
 321 the mean STF location ($\pm 2.5^\circ$ latitude band, 2004-2019). Chl-a anomalies are extract between the
 322 mean Argo STF location and 5° south of it. Observations and model results have been binned to 5°
 323 longitude bins.

324 3.3. Observed trends in STF location from Argo SST and Chl-a between 2004 to 2019

325 Based on the concept outlined above, a southward shift of the westerly winds would promote a
 326 southward shift of the STF, while stronger westerly winds will increase the northward Ekman transport
 327 and initiate a northward shift of the STF (see Figure 1 and section 3.1). The consequence of these
 328 factors combined could be that the STF does not shift if both factors balance each other.

329 The Argo STF trends are mostly small ($< 0.25^\circ$ latitude per decade, black line in Figure 4a), but show a
 330 predominantly southward directed trend following the southward shifted westerly winds. Larger
 331 southwards trends ($> 0.5^\circ$ latitude per decade) are seen between 70°E to 105°E , 130°E - 160°W and
 332 between 180 and 160°E . The southward shift of the STF goes along with positive Chl-a trends south of
 333 the mean location of the Argo STF (green line), as expected with the concept proposed in Figure 1 (red
 334 bar in Figure 4a). Nevertheless, the actual Argo STF trends are smaller than the expected STF trend,
 335 based on the changes in the position of the zero wind stress curl (Qu et al. 2018) and the location of
 336 the maximum westerly winds (Figure S1d), which both show a southward trend of $\sim 0.4^\circ$
 337 latitude/decade. We argue that this mis-match, between expected and actual STF trends, is related to
 338 changes in local winds (i.e. zonal wind, blue line) and the consequential Ekman forcing. In regions
 339 where the zonal wind trend is positive over the STF, the observed STF trend is smaller than the
 340 expected STF trend (-0.4° latitude/decade) and conversely for negative zonal wind trends. Regions
 341 which follow this concept are shown by the purple bar in Figure 4a and align with regions of alignment
 342 identified in the previous sections. Exceptions from the concept again match with regions of elevated
 343 eddy variability, where the STF encounters currents.



344 Figure 4. (a) Trends in the meridional location of the STF based on Argo SST data from 2004-2019
 345 (black line) and trends in Chl-a concentrations (green line). Zonal wind trends are extracted over the
 346 mean location of the STF ($\pm 2.5^\circ$ latitude band, 2004-2019), while the Chl-a trends are the average Chl-
 347 a anomaly over a 5° latitude band south of the mean STF location. The red bar at the top indicates
 348 regions where the STF trend and Chl-a trend have the opposite sign. The purple bar indicates regions
 349 where zonal wind trends can explain the observed STF trend in relation to the expected STF trend ($-$
 350 0.4° latitude/decade, indicate by the grey dashed line). (b) Zonal wind trend from JRA-55-DO from
 351 2004-2019 is shown by the color shading and Argo mean STF location by the black line. The blue line
 352 in 4a is based on this trend over the STF.
 353

354 The observed southward trend of the STF goes in hand with a poleward habitat expansion of
355 subtropical species (Law et al. 2017; Shears and Bowen 2017) and is related to the observed poleward
356 expansion of the subtropical gyres (Yang et al. 2020). In this context accelerated warming over the
357 western boundary currents has been observed (Wu et al. 2012) and had cascading effects on the
358 marine ecosystems via marine heatwaves (Smale et al. 2019). Our results together with others (e.g.
359 Del Castillo et al. (2019), Carranza and Gille (2015); Montie et al. (2020)) suggest an increase in
360 biological productivity in the Southern Ocean over the past decades, based on increasing Chl-a
361 concentrations and a positive link to temperature. This increase has implications for the foodweb, and
362 the fisheries of the STF. However, how these Chl-a trends will impact fish, fisheries, and the biological
363 carbon pump is complex and not well understood. Nevertheless, future climate projections suggest
364 that southernmost western boundary currents will further intensify (Qu et al. 2019; Sen Gupta et al.
365 2021), subtropical gyres will continue to expand poleward (Yang et al. 2020) and marine heatwaves
366 will become more intense and frequent and impact the STF (Behrens et al. 2022; Oliver et al. 2019).
367 More research is needed to robustly quantify the impacts of these physical changes on the biology
368 and the ecosystems associated with the STF.

369 **4. Conclusions**

370 This paper explores how changes in surface winds can alter the location of the STF. We have tested
371 how a southerly shift, or an increase of the westerly winds over the Southern Ocean can impact the
372 meridional location of the STF. We tested if and where Ekman dynamics can be applied to explain the
373 meridional shift in the STF and in which regions other drivers control the response.

374 In two sensitivity simulations a trend pattern to surface winds was applied over a 20-year period to
375 investigate the transient response to these wind anomalies. The results from the sensitivity
376 simulations and analyses of the past observed STF variability over the last 20 years have demonstrated
377 that STF shifts, away from ocean currents, can be explained in the first-instance by changes in the
378 Ekman transports as a consequence of the zonal wind stress anomalies over the STF ($\pm 2.5^\circ$ longitude).
379 Stronger westerly winds increase the northward Ekman transport and cause the STF to shift
380 northward. Southward shifted winds, which results in locally reduced westerly winds reduces the
381 Ekman transport and the STF shifts southward. However, the actual magnitude of the meridional
382 displacement depends strongly on the local conditions (e.g., oceanic currents, stratification, and
383 meridional temperature gradient). Nevertheless, regions where Ekman transport anomalies are
384 largest tend to show the larger meridional displacements. The STF does not follow the Ekman response
385 in regions where it interacts with ocean boundary currents. In these boundary current regions the STF
386 is dominated by the Sverdrup balance and increases in westerly winds push the STF southward despite
387 positive Ekman anomalies, as the strength of the boundary currents increases and offsets the Ekman
388 forces. Other exceptions are regions where mesoscale eddy activity is high. In these regions the STF
389 does not show robust links with Ekman transport anomalies.

390 Over the period 2004-2019 the observed southward trend of the STF is less than the expected
391 southward trend in most regions, based on the overall southward shift of the zero wind stress curl and
392 maximum in zonal winds, which both show a southward trend of 0.4° latitude per decade. We argue
393 that the discrepancy between expected and actual shift of the STF can be explained by trends in the
394 Ekman forcing, which are asymmetric and oppose the southward trend caused by the shift in some
395 regions. The regions where local Ekman transports cannot explain the actual shift of the STF are very
396 consistent between interannual and decade timescales and align with regions of mesoscale variability
397 and strong oceanic currents such as in the vicinity of western boundary currents.

398 Changes in the location of the STF have profound implications on Chl-a concentrations, which provides
399 motivation to improve our understanding about the physical driver of these STF shifts. A southward
400 shifted STF generates negative Chl-a anomalies north of its previous STF position and negative Chl-a
401 anomalies to its north, with implications on the local ecosystem and carbon fluxes. While the sign of
402 the Chl-a anomalies follows the direction of the STF shift, the magnitude of the Chl-a anomalies does
403 not necessarily correspond to the magnitude of the STF shift. Here, the local conditions (e.g., nutrient
404 concentrations) are important. Nevertheless, the impact on boundary current transports and Chl-a
405 might be more nuanced due to the asymmetry of wind trends over the Southern Ocean (Beal and
406 Elipot 2016; Goyal et al. 2021; Noh et al. 2021; Sallée et al. 2010; Waugh et al. 2020), which results in
407 regional variations. Here more regional studies are needed to understand the local response.

408 **5. Acknowledgements**

409 This paper obtained funding and support through the Royal Society Marsden Fund (NIW1701) and
410 funding from the Ministry of Business, Innovation and Employment through the Deep South National
411 Science Challenge (C01X1902). We would like to acknowledge the collaboration with MetOffice (UK)
412 and the NeSI High Performance Computing Facility team for their technical support. Finally, I would
413 like to acknowledge my partner, son, and daughter. Data used for this study can be freely accessed
414 through: <https://doi.org/10.5281/zenodo.6837010> .

415

416 **6. References**

- 417 Barnier, B., and Coauthors, 2006: Impact of partial steps and momentum advection schemes in a
418 global ocean circulation model at eddy-permitting resolution. *Ocean Dynam*, **56**, 543-567.
- 419 Beal, L. M., and S. Elipot, 2016: Broadening not strengthening of the Agulhas Current since the early
420 1990s. *Nature*, **540**, 570-+.
- 421 Behrens, E., A. M. Hogg, M. H. England, and H. Bostock, 2021: Seasonal and Interannual Variability of
422 the Subtropical Front in the New Zealand Region. *Journal of Geophysical Research: Oceans*, **126**,
423 e2020JC016412.
- 424 Behrens, E., G. Rickard, O. Morgenstern, T. Martin, A. Osprey, and M. Joshi, 2016: Southern Ocean
425 deep convection in global climate models: A driver for variability of subpolar gyres and Drake
426 Passage transport on decadal timescales. *Journal of Geophysical Research: Oceans*, **121**, 3905--3925.
- 427 Behrens, E., G. Rickard, S. Rosier, J. Williams, O. Morgenstern, and D. Stone, 2022: Projections of
428 Future Marine Heatwaves for the Oceans Around New Zealand Using New Zealand's Earth System
429 Model. *Frontiers in Climate*, **4**.
- 430 Belkin, I. M., 2021: Subtropical Frontal Zone of the Southern Ocean.
- 431 Belkin, I. M., and A. L. Gordon, 1996: Southern Ocean fronts from the Greenwich meridian to
432 Tasmania. *J Geophys Res-Oceans*, **101**, 3675-3696.
- 433 Carranza, M. M., and S. T. Gille, 2015: Southern Ocean wind-driven entrainment enhances satellite
434 chlorophyll-a through the summer. *Journal of Geophysical Research: Oceans*, **120**, 304-323.
- 435 Chapman, C. C., M.-A. Lea, A. Meyer, J.-B. Sallée, and M. Hindell, 2020: Defining Southern Ocean
436 fronts and their influence on biological and physical processes in a changing climate. *Nature Climate
437 Change*, **10**, 209-219.
- 438 Chiswell, S. M., J. Bradford-Grieve, M. G. Hadfield, and S. C. Kennan, 2013: Climatology of surface
439 chlorophylla, autumn-winter and spring blooms in the southwest Pacific Ocean. *Journal of
440 Geophysical Research: Oceans*, **118**, 1003-1018.
- 441 De Boer, A. M., R. M. Graham, M. D. Thomas, and K. E. Kohfeld, 2013: The control of the Southern
442 Hemisphere Westerlies on the position of the Subtropical Front. *Journal of Geophysical Research:
443 Oceans*, **118**, 5669-5675.
- 444 Deacon, G. E. R., 1982: Physical and Biological Zonation in the Southern-Ocean. *Deep-Sea Res*, **29**, 1-
445 15.

446 Debreu, L., C. Vouland, and E. Blayo, 2008: AGRIF: Adaptive grid refinement in Fortran. *Computers &*
447 *Geosciences*, **34**, 8-13.

448 Del Castillo, C. E., S. R. Signorini, E. M. Karaköylü, and S. Rivero-Calle, 2019: Is the Southern Ocean
449 Getting Greener? *Geophysical Research Letters*, **46**, 6034-6040.

450 Frankcombe, L. M., P. Spence, A. M. Hogg, M. H. England, and S. M. Griffies, 2013: Sea level changes
451 forced by Southern Ocean winds. *Geophysical Research Letters*, **40**, 5710-5715.

452 Good, S. A., M. J. Martin, and N. A. Rayner, 2013: EN4: Quality controlled ocean temperature and
453 salinity profiles and monthly objective analyses with uncertainty estimates. *Journal of Geophysical*
454 *Research: Oceans*, **118**, 6704--6716.

455 Goyal, R., M. H. England, M. Jucker, and A. Sen Gupta, 2021: Response of Southern Hemisphere
456 Western Boundary Current Regions to Future Zonally Symmetric and Asymmetric Atmospheric
457 Changes. *Journal of Geophysical Research: Oceans*, **126**.

458 Graham, R. M., A. M. de Boer, K. J. Heywood, M. R. Chapman, and D. P. Stevens, 2012: Southern
459 Ocean fronts: Controlled by wind or topography? *J Geophys Res-Oceans*, **117**, C08018.

460 Hunke, E. C., and W. H. Lipscomb, 2010: CICE: The Los Alamos Sea Ice Model, Documentation and
461 Software User's Manual, Version 4.1.

462 Law, C. S., G. J. Rickard, S. E. Mikaloff-Fletcher, M. H. Pinkerton, E. Behrens, S. M. Chiswell, and K.
463 Currie, 2017: Climate change projections for the surface ocean around New Zealand. *New Zeal J Mar*
464 *Fresh*, 1--27.

465 Lenn, Y.-D., and T. K. Chereskin, 2009: Observations of Ekman currents in the Southern Ocean. *J Phys*
466 *Oceanogr*, **39**, 768-779.

467 Lovenduski, N. S., 2005: Impact of the Southern Annular Mode on Southern Ocean circulation and
468 biology. *Geophysical Research Letters*, **32**, L11603.

469 Madec, G., and Coauthors, 2017: NEMO ocean engine.

470 Montie, S., M. S. Thomsen, W. Rack, and P. A. Broady, 2020: Extreme summer marine heatwaves
471 increase chlorophyll a in the Southern Ocean. *Antarctic Science*, **32**, 508-509.

472 Noh, K. M., H.-G. Lim, and J.-S. Kug, 2021: Zonally asymmetric phytoplankton response to the
473 Southern annular mode in the marginal sea of the Southern ocean. *Scientific Reports*, **11**, 10266.

474 Oliver, E. C. J., and Coauthors, 2019: Projected Marine Heatwaves in the 21st Century and the
475 Potential for Ecological Impact. *Frontiers in Marine Science*, **6**.

476 Orsi, A. H., T. Whitworth, and W. D. Nowlin, 1995: On the Meridional Extent and Fronts of the
477 Antarctic Circumpolar Current. *Deep-Sea Res Pt I*, **42**, 641-673.

478 Pinkerton, M., K. Richardson, P. Boyd, M. Gall, J. Zeldis, M. Oliver, and R. Murphy, 2005:
479 Intercomparison of ocean colour band-ratio algorithms for chlorophyll concentration in the
480 Subtropical Front east of New Zealand. *Remote Sens Environ*, **97**, 382-402.

481 Qu, T., I. Fukumori, and R. A. Fine, 2018: Spin-up of the Southern Hemisphere Super Gyre. *Journal of*
482 *Geophysical Research: Oceans*, **124**, 2018JC014391.

483 Qu, T. D., I. Fukumori, and R. A. Fine, 2019: Spin-Up of the Southern Hemisphere Super Gyre. *J*
484 *Geophys Res-Oceans*, **124**, 154-170.

485 Roemmich, D., and J. Gilson, 2009: The 2004–2008 mean and annual cycle of temperature, salinity,
486 and steric height in the global ocean from the Argo Program. *Progress in Oceanography*, **82**, 81--100.

487 Sallée, J. B., K. G. Speer, and S. R. Rintoul, 2010: Zonally asymmetric response of the Southern Ocean
488 mixed-layer depth to the Southern Annular Mode. *Nature Geoscience*, **3**, 273-279.

489 Sathyendranath, S., and Coauthors, 2019: An Ocean-Colour Time Series for Use in Climate Studies:
490 The Experience of the Ocean-Colour Climate Change Initiative (OC-CCI). *Sensors-Basel*, **19**.

491 Sen Gupta, A., A. Stallema, G. M. Pontes, A. S. Taschetto, A. Vergés, and V. Rossi, 2021: Future
492 changes to the upper ocean Western Boundary Currents across two generations of climate models.
493 *Scientific Reports*, **11**.

494 Shears, N. T., and M. M. Bowen, 2017: Half a century of coastal temperature records reveal complex
495 warming trends in western boundary currents. *Scientific Reports*, **7**, 14527.

496 Smale, D. A., and Coauthors, 2019: Marine heatwaves threaten global biodiversity and the provision
497 of ecosystem services. *Nature Climate Change*, **9**, 306-312.

498 Sokolov, S., and S. R. Rintoul, 2009: Circumpolar structure and distribution of the Antarctic
499 Circumpolar Current fronts: 1. Mean circumpolar paths. *J Geophys Res-Oceans*, **114**, C11018.

500 Spence, P., J. C. Fyfe, A. Montenegro, and A. J. Weaver, 2010: Southern Ocean Response to
501 Strengthening Winds in an Eddy-Permitting Global Climate Model. *Journal of Climate*, **23**, 5332-5343.

502 Spence, P., S. M. Griffies, M. H. England, A. M. Hogg, O. a. Saenko, and N. C. Jourdain, 2014: Rapid
503 subsurface warming and circulation changes of Antarctic coastal waters by poleward shifting winds.
504 *Geophysical Research Letters*, **41**, 4601--4610.

505 Storkey, D., and Coauthors, 2018: UK Global Ocean GO6 and GO7: a traceable hierarchy of model
506 resolutions. *Geoscientific Model Development*, **11**, 3187-3213.

507 Sullivan, C. W., K. R. Arrigo, C. R. McClain, J. C. Comiso, and J. Firestone, 1993: Distributions of
508 Phytoplankton Blooms in the Southern-Ocean. *Science*, **262**, 1832-1837.

509 Swart, N. C., and J. C. Fyfe, 2012: Observed and simulated changes in the Southern Hemisphere
510 surface westerly wind-stress. *Geophysical Research Letters*, **39**, n/a--n/a.

511 Thompson, A. F., and J.-B. Sallée, 2012: Jets and Topography: Jet Transitions and the Impact on
512 Transport in the Antarctic Circumpolar Current. *J Phys Oceanogr*, **42**, 956-972.

513 Tilburg, C. E., H. E. Hurlburt, J. J. O'Brien, and J. F. Shriver, 2002: Remote topographic forcing of a
514 baroclinic western boundary current: An explanation for the Southland Current and the pathway of
515 the subtropical front east of New Zealand. *J Phys Oceanogr*, **32**, 3216-3232.

516 Tsujino, H., and Coauthors, 2018: JRA-55 based surface dataset for driving ocean-sea-ice models
517 (JRA55-do). *Ocean Modelling*, **130**, 79-139.

518 Wang, W., and R. X. Huang, 2004: Wind energy input to the Ekman layer. *J Phys Oceanogr*, **34**, 1267-
519 1275.

520 Waugh, D. W., A. Banerjee, J. C. Fyfe, and L. M. Polvani, 2020: Contrasting Recent Trends in Southern
521 Hemisphere Westerlies Across Different Ocean Basins. *Geophysical Research Letters*, **47**,
522 e2020GL088890.

523 Weeks, S. J., and F. A. Shillington, 1994: Interannual scales of variation of pigment concentrations
524 from coastal zone color scanner data in the Benguela Upwelling system and the Subtropical
525 Convergence zone south of Africa. *Journal of Geophysical Research: Oceans*, **99**, 7385-7399.

526 Wu, L., and Coauthors, 2012: Enhanced warming over the global subtropical western boundary
527 currents. *Nature Climate Change*, **2**, 161--166.

528 Yang, H., and Coauthors, 2020: Poleward Shift of the Major Ocean Gyres Detected in a Warming
529 Climate. *Geophysical Research Letters*, **47**.

530